ACS APPLIED MATERIALS & INTERFACES

Research Article

Cite This: ACS Appl. Mater. Interfaces 2019, 11, 45057−45067

www.acsami.org

In Situ Optical and Stress Characterization of Alloyed Pd_xAu_{1-x} Hydrides

Kevin J. Palm,[†,‡] Joseph B. Murray,[‡] Joshua P. McClure,[⊥] Marina S. Leite,[‡,§,△] and Jeremy N. Munday*[,‡,∥,▲]

[†]Department of Physics, [‡]Institute for Research in Electronics and Applied Physics, [§]Department of Materials Science and Engineering, and [∥]Department of Electrical and Computer Engineering, University of Maryland, College Park, Maryland 20742, United States

[⊥]Sensors and Electron Devices Directorate, U.S. Army Research Laboratory, 2800 Powder Mill Road, Adelphi, Maryland 20783-1197, United States

Supporting Information

ABSTRACT: Pd_xAu_{1-x} alloys have recently shown great promise for next-generation optical hydrogen sensors due to their increased chemical durability while their optical sensitivity to small amounts of hydrogen gas is maintained. However, the correlation between chemical composition and the dynamic optical behavior upon hydrogenation/dehydrogenation is currently not well understood. A complete understanding of this relation is necessary to optimize future sensors and nanophotonic devices. Here, we quantify the dynamic optical, chemical, and mechanical properties of thin film Pd_xAu_{1-x} alloys as they are exposed to H_2 by combining in situ ellipsometry with gravimetric and stress measurements. We demonstrate the dynamic optical property dependence of the film upon hydrogenation and directly correlate it with the hydrogen content up to a maximum of 7 bar of H_2. With this measurement, we find that the thin films exhibit their strongest optical sensitivity to H_2 in the near-infrared. We also discover higher hydrogen-loading amounts as compared to previous measurements for alloys with low atomic percent Pd. Specifically, a measurable optical and gravimetric hydrogen response in alloys as low as 34% Pd is found, when previous works have suggested a disappearance of this response near 55% Pd. This result suggests that differences in film stress and microstructuring play a crucial role in the sorption behavior. We directly measure the thin film stress and morphology upon hydrogenation and show that the alloys have a substantially higher relative stress change than pure Pd, with the pure Pd data point falling 0.9 GPa below the expected trend line. Finally, we use the measured optical properties to illustrate the applicability of these alloys as grating structures and as a planar physical encryption scheme, where we show significant and variable changes in reflectivity upon hydrogenation. These results lay the foundation for the composition and design of next-generation hydrogen sensors and tunable photonic devices.

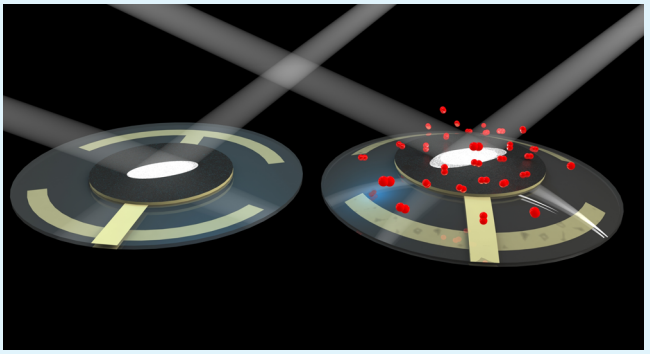

KEYWORDS: *hydride, metal alloys, Pd, Au, optical properties, stress, thin film*

INTRODUCTION

The alloying of different metals to finely tune optical and material properties has allowed for great advancements in a wide variety of applications from plasmonic sensors to catalysts.[1−8] Alloying creates opportunities to improve the material characteristics beyond that of the pure metal components. Furthermore, one can combine the desirable optical and structural properties from different metals into a single alloy. This process is particularly advantageous when applied to metal hydrides, where the optical properties, electric properties, and response to H_2 gas are all of interest.

Metal hydrides are useful for a wide range of applications, including color displays, switchable mirrors, and tunable plasmonics.[9−16] Moreover, metal hydrides possess the capability to store and detect hydrogen. The opportunity to use hydrogen for energy storage and distribution is becoming more attractive, and with a push for a future hydrogen economy, more high-quality sensors are needed to mitigate the dangers of hydrogen leaks. All-optical hydrogen sensors are the preferred method of detection due to the decreased risk of ignition. This is in contrast to more traditional electrical sensors, which have the potential to spark upon device malfunction. These optical sensors are required to have fast response times, resistance to surface poisoning, limited

Received: August 9, 2019
Accepted: October 31, 2019
Published: October 31, 2019

DOI: 10.1021/acsami.9b14244
ACS Appl. Mater. Interfaces 2019, 11, 45057−45067

intracycle hysteresis between hydrogen absorption and desorption cycles, and a large enough signal to be reliably read.[17]

Pd has been the standard metal investigated for hydrogen sensing and storage because it is the only pure metal that can absorb and desorb hydrogen from its lattice at room temperature without an activation layer.[18] However, pure Pd suffers from slow response times, surface poisoning, and a large hysteresis.[19,20] Alloying Pd with other metals has been shown as a solution to mitigate these problems, particularly alloying with Au.[6,7,21−25] In addition to these improved hydrogen-sensing properties, Pd_xAu_{1-x} alloys have been of particular interest for improving catalysis reactions,[1,5,26−28] as well as being used as a hydrogen separation membrane.[29,30] A more complete characterization is essential to facilitate further use of these alloys.

In this paper, we quantify the changes in the optical, mechanical, and chemical properties of seven different Pd_xAu_{1-x} thin films as a function of hydrogenation. These alloys are fabricated by physical vapor deposition cosputtering at room temperature, a versatile process that allows for a wider variety of substrates for sensors that are not possible with fabrication methods that require high-temperature annealing steps. We simultaneously investigate the dynamic optical properties and hydrogen-loading amounts upon exposure to H_2 gas. We directly measure the optical responses with spectroscopic ellipsometry with wavelengths spanning from 225 to 1690 nm, and we identify changes in the complex refractive index upon hydrogenation. We use quartz crystal microbalance (QCM) measurements to determine the hydrogen sorption of the material and find higher loading quantities than previously reported for gas-phase loading experiments. For each hydrogen exposure, we also simultaneously measure the stress change and discover that the relative change in stress of the Pd_xAu_{1-x} alloys is 0.9 GPa higher than the change of pure Pd. Upon investigating the correlation between this stress and the change in the surface roughness of the material, we find that despite the large amount of thin film stress present in the alloys, there are no observed roughness changes for any of the films after loading. Finally, we computationally demonstrate the applicability of these alloys to enhance light reflection in grating structures as well as demonstrate a scheme for physical encryption. Our research elucidates important material properties of Pd_xAu_{1-x} alloys that will further inform hydrogen sensor design and implementation.

EXPERIMENTAL SECTION

Fabrication and Characterization of Pd_xAu_{1-x} Thin Films. The thin film Pd_xAu_{1-x} alloys are fabricated by room temperature physical vapor deposition cosputtering with Pd (99.95%) and Au (99.99%) sputtering targets. A Si chip with a lithographically defined 1×1 cm^2 area and two separate AT-cut 5 MHz QCMs were included as substrates for each deposition run. The film geometry on the QCMs was defined by a 12.5 mm diameter circular shadow mask centered on the top QCM electrode. The substrates were cleaned with acetone, methanol, and 2-propanol rinses prior to deposition (the lithographic defining of the Si piece was performed after the solvent cleaning). Prior to Pd_xAu_{1-x} deposition, the base pressure in the main chamber was maintained at less than 1.8×10^{-8} Torr. The thin film alloys were deposited at room temperature, with Ar gas introduced and adjusted to a 10 mTorr pressure. During deposition, a constant rotation of 20 rpm, a z-height of 100 mm, and a gun tilt of 7.5 mm were applied to ensure uniform chemical composition across each sample. Direct current powers ranging from 75 to 300 W were applied to alter the Pd_xAu_{1-x} composition. Two sets of samples were produced for these experiments. The first set was ∼100 nm thick and was deposited directly onto the substrates. The second set was ∼400 nm thick with a 10 nm Cr adhesion layer that was sputtered onto the substrates before the alloy deposition without breaking vacuum. The Cr was deposited with a 150 W RF source instead of a standard dc source because the only dc sources available in the system were connected to the Au and Pd targets.

The composition of each alloy was measured with energy-dispersive X-ray spectroscopy (EDX). For each sample on a Si substrate, EDX measurements were taken on four separate points to ensure uniformity. The raw EDX data are shown in Figure S1 of the Supporting Information (SI). The first set of depositions had the compositional fractions (Pd_xAu_{1-x}) of x = 0, 0.14, 0. 34, 0.42, 0.52, 0.73, and 1. For the second batch (∼400 nm thick with the Cr adhesion layer), we focused on samples with higher Pd content, having the compositions x = 0.41, 0.59, 0.73, 0.77, 0.83, 0.88, and 1.

Film thickness and roughness measurements were taken with an atomic force microscope (AFM) in an unpressurized dry air atmosphere. The roughness measurement was taken on three distinct 2×2 μm^2 patches on each of the alloys. The reported roughnesses in this paper are all root-mean-square (RMS) roughnesses and are calculated by taking the RMS value of each line of the AFM image and taking the median of these values. The film thickness measurements were taken on the lithographically defined Si samples. Scans sized 20×20 μm^2 were taken centered on the defined edge of the metal square. The step results in a bimodal Gaussian distribution for the histogram of the topography data. The sample height was taken as the difference in the mean of the two Gaussians.

Inductively coupled plasma optical emission spectroscopy (ICP-OES) was used to confirm both the sample thicknesses and the chemical composition for each of the alloys. The Si squares were dissolved in boiling aqua regia and subsequently diluted to 50 mL. ICP-OES was then used to find the Pd and Au concentrations of this solution. Using the known surface area of the alloy on the Si sample, the atomic masses, and the densities of these materials, the thickness and atomic percentage of the alloys can be calculated. These calculated values agreed within the error of the results of the EDX and AFM measurements.

Optical Property Measurements. Optical property measurements were taken with a spectroscopic ellipsometer in a custom environmental chamber as previously demonstrated by Palm et al.[31] The QCM frequency is simultaneously recorded with the optical data to correlate the hydrogen content of the sample with the optical property changes. Measurements for each alloy are made at four different angles (48°, 55°, 70°, and 75°) for the pristine metal alloy before hydrogenation. The dynamic optical properties of the alloys were then taken at 75° as the environmental chamber was switched from 7 bar of Ar to 7 bar of H_2. The 75° orientation is chosen for the dynamic measurements due to steeper incident angles having a higher sensitivity to optical changes. The measurements in the hydrogenated state were then retaken at all four angles at the end of this process. The chamber was then purged with Ar with the dynamic data being recorded again at 75°. This process was repeated for a total of four hydrogen absorption steps and three desorption steps for each alloy. Further details of the ellipsometric measurement, window compensation of the environmental chamber, and the dynamic optical fitting method can be found in the work by Palm et al.[31]

Hydrogen-Loading and Stress Measurements. The hydrogen-loading and stress measurements were taken in a separate environmental chamber equipped with an interferometer using the metal alloy films on the QCM as one of the mirrors. The loading value for each alloy is calculated with the method outlined by Murray et al.,[32] which compensates the total QCM frequency change with effects from stress along with environmental effects, such as changes in gas composition.

Because the QCM substrates used in our experiments are anisotropic, the standard way of determining thin film stress using the Stoney equation is not applicable.[33] The stress values reported in this work use an adapted method from EerNisse's double resonator

DOI: 10.1021/acsami.9b14244
ACS Appl. Mater. Interfaces 2019, 11, 45057−45067

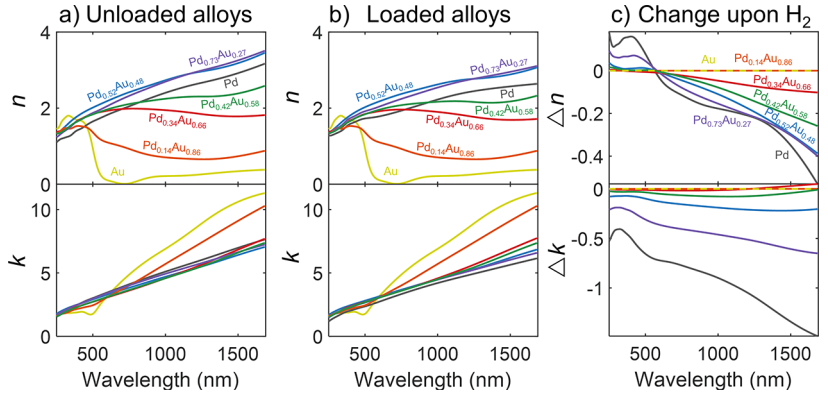

Figure 1. Measured optical properties of seven different Pd_xAu_{1-x} alloys. (a) Optical properties of each alloy without any hydrogen in the lattice (unloaded). (b) Optical properties of the hydrogenated alloys under an atmosphere of 7 bar of H_2. (c) Change in the optical properties for each alloy upon hydrogenation. Change is defined by the optical properties of the hydride subtracted from the optical properties of the unloaded metal.

model.[34] Instead of using two separate cuts of QCMs, we measure the curvature of the sample and use the curvature to frequency relation detailed by Murray et al.[32] to find the change in QCM frequency due to stress in the sample. The change in stress of the thin film upon hydrogenation is then

$$\Delta\sigma = \frac{\Delta f_s \tau_q}{K^{AT}\tau_f f_0} \quad (1)$$

where Δf_s is the change of QCM frequency due to stress, τ_q and τ_f are the thicknesses of the quartz of the QCM and the metal film respectively, f_0 is the measured QCM frequency before hydrogenation, and K^{AT} is a constant defined by EerNisse to be -2.75×10^{-12} cm^2/dyn for a 5 MHz AT-cut QCM.[34] Using this method, we assume that the stress is isotropic through the thickness of the film. All stresses reported in this paper are compressive stresses and are defined to be positive.

RESULTS AND DISCUSSION

Dynamic Optical Property Measurements. Figure 1 shows the optical properties for the seven different 100 nm alloys investigated in this study as well as their property change upon hydrogenation in 7 bar of H_2 for the wavelength range of 225−1690 nm. Because metal hydrides typically have significant dislocation formation with initial loading, the data shown here are for the second hydrogenation of the alloys. Thus, the plots describe a typical loading cycle. For the data of the initial loading of the pristine alloys and for the dielectric functions of both the first and second loads, see Figures S2 and S3 (SI), respectively. To verify our optical fitting model for these materials, we compare our measurements to the Johnson and Christy values reported for Au and Pd, which can be found in Figure S4 (SI),[35,36] and agreement was found. The non-hydrogenated optical properties of Pd_xAu_{1-x} alloys have previously been inferred with modeled electron energy loss spectroscopy (EELS) data acquired on individual nanoparticles in the range of 248−827 nm[37] as well as with reflection and transmission measurements for a single $Pd_{50}Au_{50}$ thin film alloy in the range of 350−1050 nm.[38] However, the optical properties have not been directly measured with spectroscopic ellipsometry and have not been measured deeply into the near-infrared region. Furthermore, the optical property dependence of these alloys upon hydrogenation has not yet been investigated, which we present here.

We observe a wide range of refractive indices ($n + ik$) for the alloys as we adjust the chemical composition from pure Au to pure Pd. For the imaginary part of the index (k), we find that that the five alloys with the highest atomic percent Pd have similar values and trends, with the pure Au and $Pd_{0.14}Au_{0.86}$ exhibiting higher values. This is consistent with visual observation, where the five alloys with the highest Pd content all appear to have the same reflective gray color, with the $Pd_{0.14}Au_{0.86}$ being the only alloy with a yellow hue approaching the appearance of the Au. An interesting trend is observed in the real part of the index (n), where one may expect the intermediate alloys to monotonically increase in n from the lower Au values to the higher Pd values as the Pd composition is increased. Instead, both the $Pd_{0.52}Au_{0.48}$ and the $Pd_{0.73}Au_{0.27}$ alloys have a higher n than pure Pd across the entire wavelength range investigated. The nonlinearity of the optical properties with composition is not unique to the Pd_xAu_{1-x} system but is also present in the properties of other noble-metal alloys.[8] The addition of Pd to PdAu results in a nonmonotonic and dramatic increase of the valence band at the Γ point.[1] The additional electronic states below the Fermi level resulting from the break in degeneracy of the band structure are likely responsible for extra interband transitions in these alloys and, ultimately, for the higher values of n observed.

Upon hydrogenation, pure Pd has the largest optical change in both n and k, as expected. The magnitude of the change decreases as the Pd content in the alloys is decreased. The x = 0.34 sample has the smallest atomic percent Pd in an alloy for which we observe a measurable optical change, showing a slight decrease in n but very little change in k. For both the Au and $Pd_{0.14}Au_{0.86}$, we observe no measurable response when H_2 is introduced to the system. For the pure Pd, the addition of H_2 causes a decrease in k across all wavelengths investigated, a decrease in n for wavelengths above 565 nm, and an increase below 565 nm, which agrees with the literature.[31,39] These trends are all observed in the alloys with the next three highest Pd contents. The zero change intercepts in the real part of the index occur between 550−580 nm for Pd and the alloys with the next three highest Pd compositions. The results also demonstrate that, for all alloys (and the pure Pd film), the largest response to hydrogenation occurs in the near-infrared region of the electromagnetic spectrum. This higher response at longer wavelengths has been observed with other nanostructures and metal hydrides.[6,22,31] By shifting to longer detection wavelengths, Pd_xAu_{1-x} alloys with lower x become more detectable because of their increase in responsivity. This allows for the use of alloys with higher Au concentration as sensors with their increase in antihysteresis and antipoisoning

DOI: 10.1021/acsami.9b14244
ACS Appl. Mater. Interfaces 2019, 11, 45057−45067

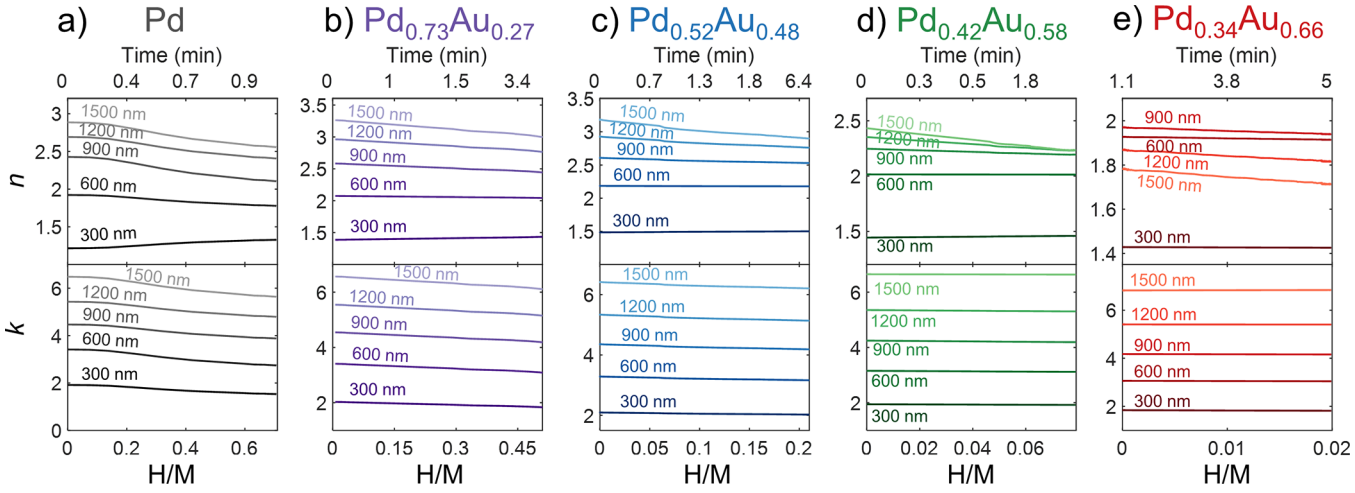

Figure 2. Optical response versus hydrogen loading. (a–e) Relationship of the optical properties (n and k) with the hydrogen content for each of the five alloys that have an interaction with H_2. Note that the top time axis has nonlinear spacing with each top tick corresponding to the time that the alloy reached the stated H/M amount. Time = 0 min is defined as the time that hydrogen is first introduced into the system.

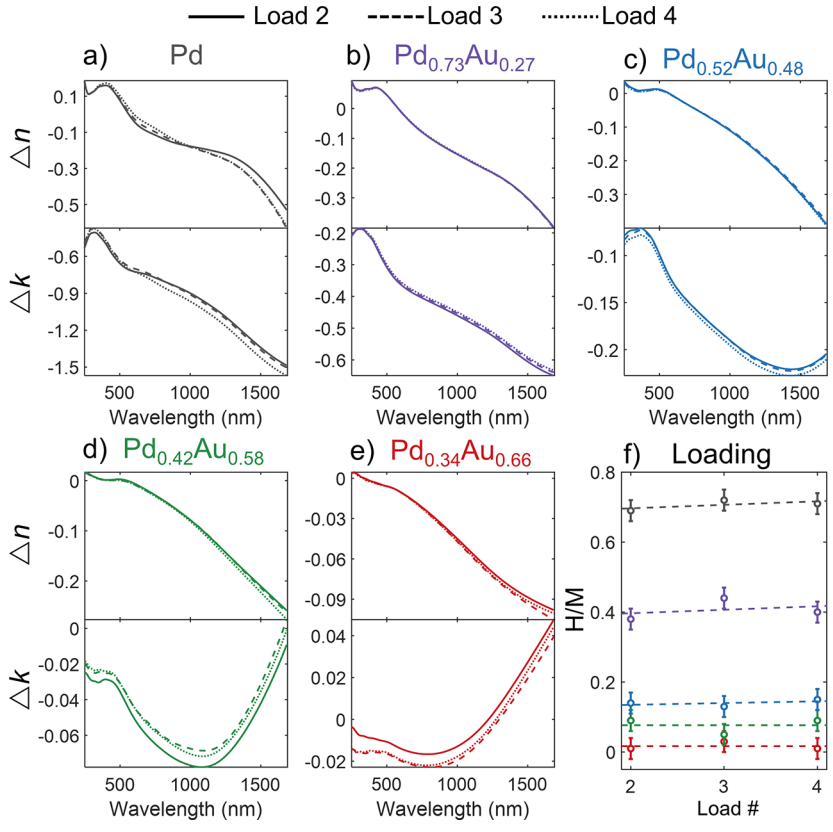

Figure 3. Hydrogen-cycling properties of alloys. (a–e) Comparison of the change in optical properties for each of the five alloys that interact with hydrogen. Δn and Δk are plotted for the second through fourth loads with the first load excluded. Δn and Δk are defined by the optical properties of the current hydride state subtracted from the values of the previously unloaded state. (f) Calculated hydrogen-loading values for the second through fourth loads. Dashed lines are linear fits for each alloy. Alloy colors match those shown in a–e, with the highest (lowest) H/M ratio corresponding to Pd ($Pd_{0.34}Au_{0.66}$).

benefits. For the full time–dynamic changes of the optical properties, see Figure S5 (SI).

In addition to the optical properties, the amount of hydrogen in the metal lattice was simultaneously monitored. Figure 2 shows the dynamic behavior of the refractive index versus hydrogen loading. We specify the amount of hydrogen by H/M, which is the amount of hydrogen atoms per metal atom in the lattice (including both Pd and Au). Figure 2 excludes the pure Au and $Pd_{0.14}Au_{0.86}$ alloy because they have no measurable reaction with H_2 either optically or gravimetrically. All other alloys share similar dynamic relationships. Each alloy has a monotonic change in optical properties with respect to loading, with the largest changes occurring in the near-infrared. For the relationship of n and k at 1500 nm with the Pd composition of the alloy and the final H/M ratio, see Figure S6 (SI). The change in optical response is nearly linear with

DOI: 10.1021/acsami.9b14244
ACS Appl. Mater. Interfaces 2019, 11, 45057–45067

loading for each of the alloys, with the Pd film appearing to have an inflection point around H/M ≈ 0.25. This behavior could be attributed to the α to β phase transition in the Pd that does not occur in the alloys with lower Pd content.[40]

We next consider the repeatability of the optical and gravimetric responses upon hydrogen cycling, which is essential for any practical device. Figure 3a–e depicts the changes in n and k for the five 100-nm-thick alloys that react with H_2 for their second through fourth H_2 exposures. As stated above, the first hydrogenation causes a slightly different optical response than the subsequent loads due to lattice defects and dislocations as it first expands.[41] After this initial disturbance, the subsequent loads cause much less of a degradation of the lattice, allowing for more consistent results. For subsequent exposures (after the first), the response is very consistent for Pd as well as the alloys. Figure 3f shows the maximum hydrogen content at 7 bar of H_2, where the amount of hydrogen in the lattice is also very consistent from load to load after the initial exposure. As expected, these results imply that any device based on Pd_xAu_{1-x} should still be pretreated with H_2 before any attempted operation. Overall, the alloys provide more consistent optical changes than the pure Pd because less hydrogen enters the lattice, causing fewer dislocations.

Material Property Measurements. To determine the exact amount of hydrogen absorbed into the metal lattice, we used a separate QCM sample in an environmental chamber that accounts for extraneous effects from stress and environmental (gas composition, pressure, temperature, etc.) changes. Figure 4 shows the relationship of the hydrogen content of the alloys at 7 bar of H_2 with the atomic percent Pd in the alloy. We can see from these measurements that the relationship follows a linear fit, as previously described in the literature.[21,22] We recorded the H/M ratio versus concentration for both the 100 nm thin films without any adhesion layer between the alloy and the Au QCM substrate and the 400 nm films with a 10 nm Cr layer between the substrate and the alloy. Both of these sets of samples follow similar linear relations within error bars. At 7 bar, our pure Pd samples had a hydrogen content of H/M = 0.72 ± 0.03 and H/M = 0.69 ± 0.03 for the 100 and 400 nm samples, respectively, which are in good agreement with previous values found in the literature.[42−44] Compared to previous gas-phase measurements on thin films, we have found higher hydrogen-loading values for the alloys, especially for the alloys with lower Pd content.[21] While previous measurements suggested no hydrogen reaction below $x \approx 0.55$ in Pd_xAu_{1-x}, we record measurable amounts of hydrogen entering the lattice down to $x = 0.34$ with a H/M value of 0.02 ± 0.01. Reasons for this higher measured loading could be contributed to different fabrication conditions of the alloys or different amounts of initial thin film stresses due to the film thickness, substrate, or the circular geometry of the film. These different intrinsic stresses can have a large effect on the material properties of the thin film system and should be characterized for each new experimental procedure.

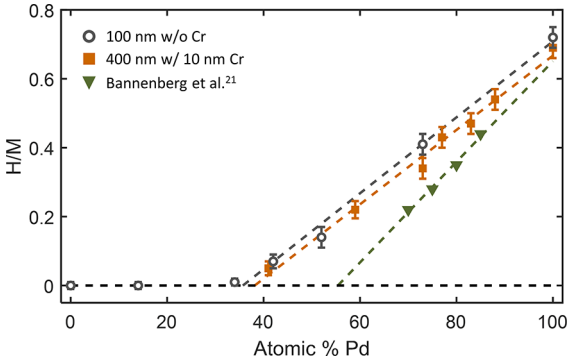

Figure 4. Total sorption data. The gray circles correspond to the 100 nm Pd_xAu_{1-x} alloy data. The gray dashed line is a linear fit of the five alloys that react with hydrogen. The solid orange squares correspond to 400 nm films that have a 10 nm Cr adhesion layer, and the orange dashed line refers to the linear fit. The measured values are compared to prior experiments by Bannenberg et al.[21] on 40-nm-thick thin films at 10 bar of H_2 partial pressure (green triangles and fit with green dashed line). The black dashed line is to guide the eye to the zero loading point.

We also performed the experiments at 0.25 bar of H_2 at 1 bar of total pressure to test the effects of driving potential on the total loading amount (see Figure S7, SI). These values are slightly lower than those taken at 7 bar, as expected due to the smaller driving potential of hydrogen in the lattice; however, the same higher than previously observed loading trend with a shallower slope when compared to atomic Pd percent is still clearly present at these lower pressures. In the literature, gas-phase loading experiments have also been performed on Pd_xAu_{1-x} nanoparticles, which exhibit a loading curve with a similar slope but lower overall values than the thin films.[21,22] Electrochemical loading experiments have also been performed on these alloys in the bulk with differing results, suggesting that a range of potential mechanisms may be at play for these different samples.[45,46]

With these unexpectedly higher loading values, we suspect that differences in film stress and microstructuring could be the cause. When thin metal films are hydrogenated, they undergo a compressive strain as the metal lattice expands to incorporate the hydrogen.[41,47−49] This strain can affect how much hydrogen can be absorbed into the lattice and can have a significant impact on the sorption kinetics.[43,50−54] Because of this effect, we investigated the amount of stress change upon hydrogenation for each of our films.

To determine the stress in our films, we measure the change in the curvature of the substrate (due to film stress) and then convert this curvature to stress using eq 1 with inputs from the simultaneous QCM data. Figure 5a shows the raw curvature changes of the 100 and 400 nm alloy samples. The 400 nm samples clearly have a much higher curvature change than the 100 nm samples, as we would expect due to there being a larger affected film mass to distribute the stress to the QCM. Once we convert this change in curvature into a change in stress (Figure 5b), we find that both the 100 and 400 nm samples have a similar relation between stress and hydrogen content.

An interesting observation from this stress relation is that neither the 100 nor 400 nm pure Pd samples fall upon the trend of the alloys (the Pd data points are excluded in the linear fits of each plot). The Pd values fall a full 0.9 GPa below the expected trend line of the stress of the alloys. This difference could be attributed to the alloys having a higher initial stress than the pure Pd due to the intrinsic strain of alloying. By starting at a higher amount of initial stress, the increase of stress per hydrogen atom is enhanced. This would cause the alloys to have a different response to hydrogen due to the different strains in the structure. This effect is an important factor in the design of future devices using Pd_xAu_{1-x}

DOI: 10.1021/acsami.9b14244
ACS Appl. Mater. Interfaces 2019, 11, 45057−45067

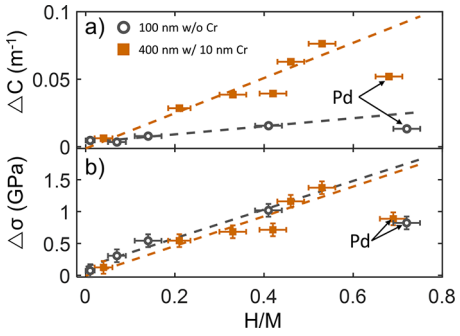

Figure 5. Stress characterization of Pd_xAu_{1-x} alloys. (a) Raw data of curvature change and (b) calculated stress values upon hydrogenation of each alloy versus the calculated final hydrogen per metal value under 7 bar of H_2. For each plot, the gray dashed line is a linear fit of the 100 nm data (gray circles) and the orange dashed line is a linear fit of the 400 nm data (orange squares), with each linear fit excluding the pure Pd data points. The vertical error bars for the curvature in part a are smaller than the marker size.

because unaccounted for stress could have deleterious effects on device performance. It is important to fully characterize the stress system down to the exact substrate and deposition temperatures; otherwise, there may be different material responses in the system, such as the higher than expected loading observed in this work. See Figure S8 (SI) for the relationship between stress and Pd alloy composition.

With these high film stresses present in the materials upon hydrogenation, we expect to see measurable changes in the surface morphology. We performed AFM scans on the alloys immediately after fabrication (i.e., before H_2 introduction), after an initial H_2 exposure, and again after a second exposure. We expect an initial increase in the surface roughness of the films after the initial hydrogenation due to the hydrogen forming dislocations and vacancies in the lattice followed by lesser changes in roughness on subsequent cycles. Instead, we found that the H_2 exposures had no measurable effect on the surface roughness of any of the films, as seen in Figure 6. We measured Pd and $Pd_{0.73}Au_{0.27}$ films for the 100 nm samples without a Cr adhesion layer and for 400 nm samples with a 10 nm Cr layer. Both sets of samples were measured on the Au QCM electrode (initial electrode RMS roughness was 1.8 nm). We also evaporated, in contrast to the sputtered samples above, a 100 nm Pd film with a 5 nm Cr adhesion layer (required to prevent delamination) to test if the roughness change was dependent on the fabrication conditions for the thin films.

Both the distribution and RMS values of the roughness remain very consistent for all sample variations (sputtering vs e-beam evaporation, 100 vs 400 nm films, Cr adhesion layer vs no adhesion layer). Figure 6a–e shows histograms of the topography data for all three scans of each material. The results are so consistent that it is difficult to distinguish between each histogram. Figure 6f–j shows the measured RMS roughnesses and Figure 6k–o shows the pristine metal topography image before the film was exposed to H_2. For each separate histogram and the corresponding topography scan, see Figure S9 (SI). The consistency of these roughness measurements are surprising due to pure Pd having a 13% volume increase upon hydrogenation and $Pd_{0.73}Au_{0.27}$ having an expected 9%

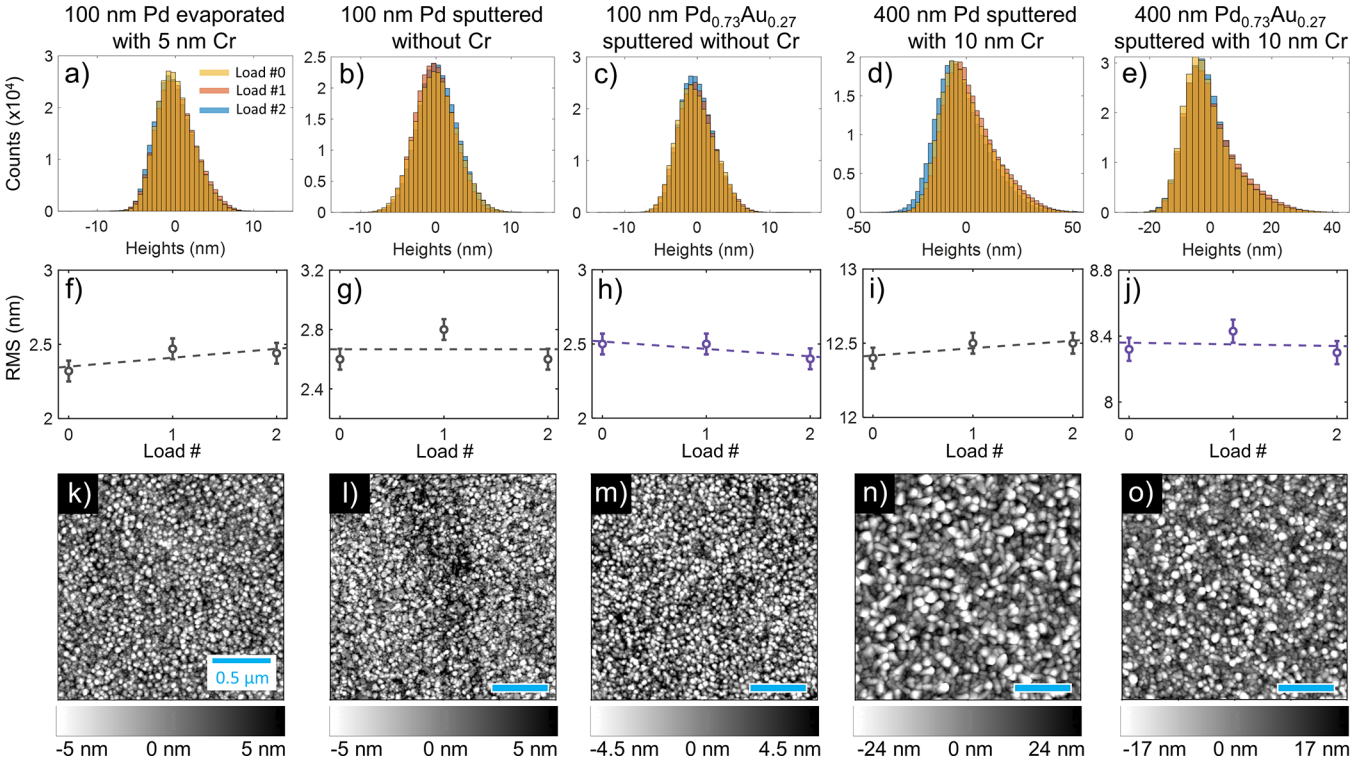

Figure 6. Pd_xAu_{1-x} thin film morphology characterization. (a–e) Histograms for each material before hydrogenation (yellow), after the first hydrogen load (orange), and after the second hydrogen load (blue). Note: histograms for first and second loadings are barely visible due to similarities with the values obtained before loading. (f–j) Calculated RMS roughness values for each load. Dashed lines are a linear fit to the data showing no significant change upon each loading cycle. (k–o) Representative AFM topography scans of the alloys before any H_2 has been introduced.

DOI: 10.1021/acsami.9b14244
ACS Appl. Mater. Interfaces 2019, 11, 45057–45067

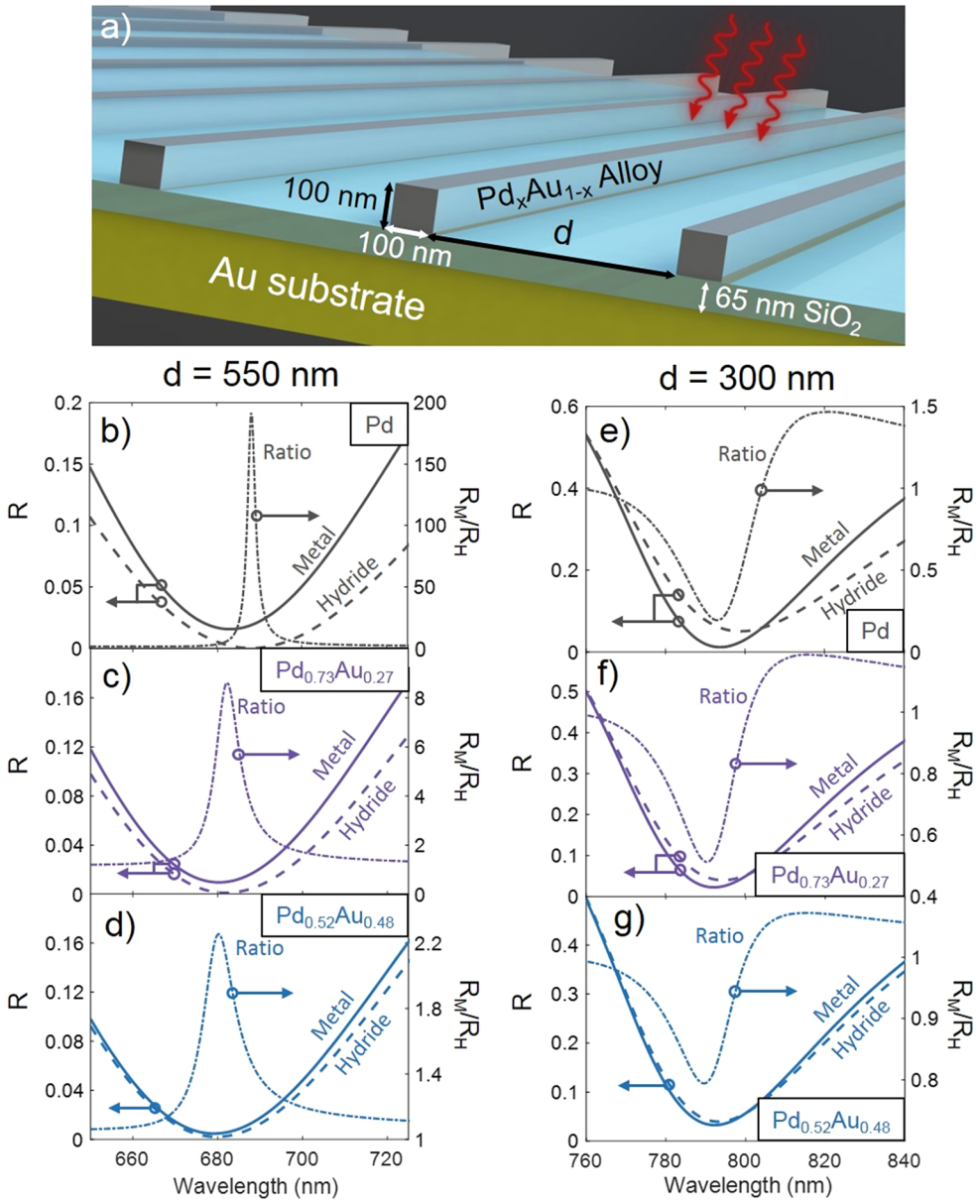

Figure 7. Simulated reflectance shifts upon hydrogenation. (a) Illustration of a simulated grating structure. Gratings are 100 nm high and 100 nm wide with a spacing *d* between gratings. A 65 nm SiO_2 spacer layer separates the grating from a Au substrate. Light is incident normally on the grating with its polarization orthogonal to the grating direction. Reflection spectra for each of the alloys with a grating periodicity of (b–d) 550 nm and (e–g) 300 nm plotted with the quotient of the metal (solid line) and hydride (dashed line) reflections showing the relative change in reflection with hydrogenation (dot dashed line).

volume increase.[41] Note that these measurements are not able to detect any vertical thickness changes, as the height set point is reset before each measurement. We do not see any difference in roughness change between the materials that are adhered directly to the QCM versus those with the Cr adhesion layer, showing that in this case the strength of the adhesion does not contribute to any roughness modification in this setup. A complete list of the measured RMS roughnesses for each of the other alloys can be found in Table S1 (SI). The data also suggest that the surface roughness of the film has no effect on the final loading amount in films of these thicknesses, as is expected. The 400 nm sputtered samples have significantly higher roughnesses than the others, yet all three Pd samples have the same total loading numbers within error bars. Similarly, the two $Pd_{0.73}Au_{0.27}$ samples also load to similar values despite differing roughnesses.

Simulations of Optical Switching. To apply these measured properties to an applicable optical switching system, we simulate (using Lumerical FDTD) several grating structures to demonstrate the opportunity of using these alloys as devices. The measured optical properties for both the metals and hydrides presented in Figure 1 are used as inputs to the simulations. Figure 7 shows the results for two separate grating structures. Both structures consist of a grating with 100 nm width and height and a 65 nm SiO_2 spacer layer on a Au substrate. This spacer layer creates a cavity effect from the reflection off the Au substrate and enables increased sensitivity.[12] We simulated two different periodicities to show the tunability of the structure. First, a 550 nm periodicity

DOI: 10.1021/acsami.9b14244
ACS Appl. Mater. Interfaces 2019, 11, 45057–45067

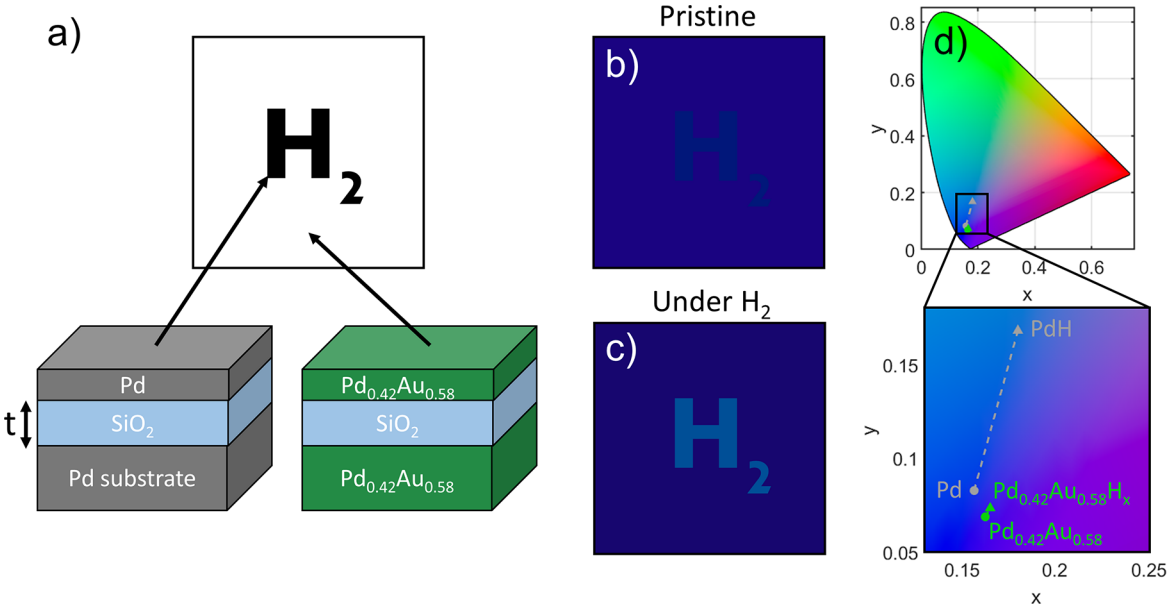

Figure 8. Physical encryption scheme. (a) Design for using Pd_xAu_{1-x} alloys in a physical encryption scheme. The "H_2" message is created using a multilayer stack containing Pd, while the background is created from a similar stack containing $Pd_{0.42}Au_{0.58}$. (b) Simulated coloring of the design before exposure to H_2 and (c) coloring of design after H_2 exposure. The SiO_2 thickness is t = 94 nm for these simulations with a 5 nm metal cap for both the active area and the background. (d) Chromaticity diagram showing the change in coloring of the lettering versus the background.

is used to obtain large spikes in the relative reflectance, where the Pd structure shows an almost 200-fold increase. As we increase the amount of Au in the alloy, we see the peak of the reflectance ratio blue shift and decrease in magnitude, with the $Pd_{0.52}Au_{0.48}$ alloys still having over a 2-fold relative increase in reflectance. By changing the periodicity of the structure to 300 nm, we can achieve the opposite response to hydrogenation, where the relative reflectance dips to well below 1 for the same materials and exposures. This demonstrates the utility of these materials for a wide range of potential photonic device designs. We note that while Pd has a larger optical response than the alloys, the $Pd_{0.73}Au_{0.27}$ and $Pd_{0.52}Au_{0.48}$ both have significant optical responses in these structures. The tunable responses combined with the chemical resistance of the alloys will allow for improved sensor design. To have an even higher sensitivity as an optical hydrogen sensor, the grating can be tuned for the resonance to occur in the near-infrared instead of the visible, because the largest optical changes upon hydrogenation occur at longer wavelengths. See Figure S10 (SI) for simulations with resonances in the infrared.

Finally, we show that these materials can be used for physical encryption and readout based on the gaseous H_2 in the environment. Previously, Mg nanostructures have been used for similar types of encryption schemes due to its large optical change with H_2.[9,55,56] In these works, e-beam lithography was used to create small and intricate encryption images. In our example, we work with thin film effects to make a macroscopic encryption scheme without the need for submicron nanostructuring. We do this by taking advantage of the similarities of the optical properties of Pd with $Pd_{0.42}Au_{0.58}$ in the non-hydrogenated state. By using the high optical sensitivity of Fabry−Perot-like resonances, we can amplify the difference in the optical responses of the two metals upon hydrogenation. Figure 8 outlines the encryption scheme of this setup. For the background of the image, there is an optically thick $Pd_{0.42}Au_{0.58}$ substrate with a 94 nm SiO_2 intermediate layer and a 5 nm $Pd_{0.42}Au_{0.58}$ capping layer. The lettering (encrypted message) is generated by using the same thickness of layers as the background structure but with Pd instead of the $Pd_{0.42}Au_{0.58}$ alloy for both the substrate and the cap. The multilayer resonance causes the coloring of the structure. Figure 8b shows the true color image of the structure containing both the lettering and background before hydrogenation. These colors are calculated using the transfer matrix method with the optical properties presented in Figure 1 as inputs. Note that all regions have indistinguishable colorings, hiding the message under ambient atmosphere. Once the structure is exposed to H_2, the Pd lettering has a large optical change as it hydrides, causing a shift in the resonance, corresponding to an observed color shift. The $Pd_{0.42}Au_{0.58}$ background, on the other hand, has a limited response to the H_2 gas, causing a minimal color change of the substrate, as seen in Figure 8c. This allows for the lettering to become visible, revealing the message. Because these materials are fully reversible as well, all one needs to do to re-encrypt the message is to remove the structure from the H_2 atmosphere. This allows for a full encryption scheme while only needing a small amount of H_2 gas to reveal the message with no other optical setup required. One note is that both sides of these structures would have to be exposed to hydrogen in order to fully hydride the Pd and $Pd_{0.42}Au_{0.58}$ layers. While the optical contrast between the two regions is relatively small, the planar nature of the structure (without need for nanofabrication) is advantageous.

CONCLUSIONS

In conclusion, we have directly measured the optical, sorption, and stress properties of a series of Pd_xAu_{1-x} alloys with controlled chemical composition upon hydrogenation. We implemented in situ spectroscopic ellipsometry from the mid-ultraviolet to the near-infrared regions and showed the consistency of these properties through multiple H_2 exposures after an initial hydrogenation. We found that our alloys exhibited a linear relation between Pd composition and

DOI: 10.1021/acsami.9b14244
ACS Appl. Mater. Interfaces 2019, 11, 45057−45067

hydrogen-loading amount, in agreement with previous reports. However, we measured a much smaller slope with respect to Pd composition than previously observed, with higher loadings obtained in alloys with lower atomic percent Pd. We postulate that this difference is caused by different thin film stresses present in our system. We characterized these stresses and found that the Pd_xAu_{1-x} alloys have a 0.9 GPa higher relative stress than measured for pure Pd, which must be accounted for in device design. Surprisingly, even with these high stress amounts, there was no observed roughness (morphology) change in the alloys when hydrogenated. Using our measured optical properties, we showed the applicability of these alloys as grating devices, where the reflectivity can either be increased or decreased upon hydrogenation, depending on the periodicity of the grating. Furthermore, we demonstrate their potential for use in a physical encryption scheme with no need for submicron nanostructuring.

Our results will further inform future sensor design, which must consider differences in fabrication methodology and the subsequent inherent stresses in the devices in order to accurately describe the sorption/optical response. We have shown that different fabrication conditions and substrate choice can alter the stress of the system, which can be used to increase the response of new devices and allow for alloys with lower Pd composition than previously expected to be utilized in the proper sensor design. We have also shown that moving to infrared sensing schemes could increase the sensitivity of these alloyed sensors when compared to the visible measurements. Future work will entail investigating new combinations of metals for potential improvements in sensing ability while maintaining chemical durability, potentially by moving from binary to ternary alloys.

■ ASSOCIATED CONTENT

Supporting Information

The Supporting Information is available free of charge on the ACS Publications website at DOI: 10.1021/acsami.9b14244.

> Figures illustrating EDX data for fabricated Pd_xAu_{1-x} alloys, initial optical properties and property changes of pristine alloys, dielectric functions and their changes upon first and second hydrogenations, optical property comparison to literature values for Au and Pd, dynamic optical properties, infrared optical properties compared with total loading, low-pressure hydrogen-loading data, stress versus Pd composition data, individual roughness plots and histograms, and infrared grating simulations and a table of compiled roughnesses (PDF)

■ AUTHOR INFORMATION

Corresponding Author

*E-mail: jnmunday@ucdavis.edu.

ORCID

Kevin J. Palm: 0000-0003-4066-4584
Joshua P. McClure: 0000-0002-2442-1139
Marina S. Leite: 0000-0003-4888-8195
Jeremy N. Munday: 0000-0002-0881-9876

Present Addresses

△M.S.L.: Department of Materials Science and Engineering, University of California, Davis, California 95616, United States

▲J.N.M.: Department of Electrical and Computer Engineering, University of California, Davis, California 95616, United States

Notes

The authors declare no competing financial interest.

■ ACKNOWLEDGMENTS

This material is based upon work supported by Google LLC and Tier 1 seed funding from the University of Maryland College Park. K.J.P is supported by a National Defense Science and Engineering Graduate Fellowship. M.S.L. is thankful for the financial support from the National Science Foundation (DMR award 16-09414). J.P.M. gratefully acknowledge the U.S. Department of the Army and U.S. Army Material Command (AMC) for supporting this work. The authors acknowledge support from the Fablab at the Maryland Nanocenter and Dr. Tarun Narayan, Dr. David Fork, Dr. Ross Kongingstein, and Matt Trevithick for their contributions to the design and qualification of the hydrogenation measurement apparatus.

■ REFERENCES

(1) McClure, J. P.; Boltersdorf, J.; Baker, D. R.; Farinha, T. G.; Dzuricky, N.; Villegas, C. E. P.; Rocha, A. R.; Leite, M. S. Structure−Property−Performance Relationship of Ultrathin Pd−Au Alloy Catalyst Layers for Low-Temperature Ethanol Oxidation in Alkaline Media. *ACS Appl. Mater. Interfaces* **2019**, *11*, 24919.

(2) Dias, M. R. S.; Gong, C.; Benson, Z. A.; Leite, M. S. Lithography-Free, Omnidirectional, CMOS-Compatible AlCu Alloys for Thin-Film Superabsorbers. *Adv. Opt. Mater.* **2018**, *6* (2), 1700830.

(3) Gong, C.; Kaplan, A.; Benson, Z. A.; Baker, D. R.; McClure, J. P.; Rocha, A. R.; Leite, M. S. Band Structure Engineering by Alloying for Photonics. *Adv. Opt. Mater.* **2018**, *6* (17), 1800218.

(4) Darmadi, I.; Nugroho, F. A. A.; Kadkhodazadeh, S.; Wagner, J. B.; Langhammer, C. Rationally Designed PdAuCu Ternary Alloy Nanoparticles for Intrinsically Deactivation-Resistant Ultrafast Plasmonic Hydrogen Sensing. *ACS Sens.* **2019**, *4*, 1424−1432.

(5) Zheng, Z.; Tachikawa, T.; Majima, T. Plasmon-Enhanced Formic Acid Dehydrogenation Using Anisotropic Pd−Au Nanorods Studied at the Single-Particle Level. *J. Am. Chem. Soc.* **2015**, *137* (2), 948−957.

(6) Nugroho, F. A. A.; Darmadi, I.; Cusinato, L.; Susarrey-Arce, A.; Schreuders, H.; Bannenberg, L. J.; da Silva Fanta, A. B.; Kadkhodazadeh, S.; Wagner, J. B.; Antosiewicz, T. J.; Hellman, A.; Zhdanov, V. P.; Dam, B.; Langhammer, C. Metal−Polymer Hybrid Nanomaterials for Plasmonic Ultrafast Hydrogen Detection. *Nat. Mater.* **2019**, *18*, 489.

(7) Wadell, C.; Nugroho, F. A. A.; Lidström, E.; Iandolo, B.; Wagner, J. B.; Langhammer, C. Hysteresis-Free Nanoplasmonic Pd−Au Alloy Hydrogen Sensors. *Nano Lett.* **2015**, *15* (5), 3563−3570.

(8) Rebello Sousa Dias, M.; Leite, M. S. Alloying: A Platform for Metallic Materials with On-Demand Optical Response. *Acc. Chem. Res.* **2019**, *52*, 2881−2891.

(9) Duan, X.; Kamin, S.; Liu, N. Dynamic Plasmonic Colour Display. *Nat. Commun.* **2017**, *8*, 14606.

(10) Sterl, F.; Strohfeldt, N.; Walter, R.; Griessen, R.; Tittl, A.; Giessen, H. Magnesium as Novel Material for Active Plasmonics in the Visible Wavelength Range. *Nano Lett.* **2015**, *15* (12), 7949−7955.

(11) Huiberts, J. N.; Griessen, R.; Rector, J. H.; Wijngaarden, R. J.; Dekker, J. P.; de Groot, D. G.; Koeman, N. J. Yttrium and Lanthanum Hydride Films with Switchable Optical Properties. *Nature* **1996**, *380* (6571), 231−234.

(12) Tittl, A.; Mai, P.; Taubert, R.; Dregely, D.; Liu, N.; Giessen, H. Palladium-Based Plasmonic Perfect Absorber in the Visible Wavelength Range and Its Application to Hydrogen Sensing. *Nano Lett.* **2011**, *11* (10), 4366−4369.

DOI: 10.1021/acsami.9b14244
ACS Appl. Mater. Interfaces 2019, 11, 45057−45067

(13) Duan, X.; Kamin, S.; Sterl, F.; Giessen, H.; Liu, N. Hydrogen-Regulated Chiral Nanoplasmonics. *Nano Lett.* **2016**, *16* (2), 1462−1466.
(14) Richardson, T. J.; Slack, J. L.; Armitage, R. D.; Kostecki, R.; Farangis, B.; Rubin, M. D. Switchable Mirrors Based on Nickel−Magnesium Films. *Appl. Phys. Lett.* **2001**, *78* (20), 3047−3049.
(15) Borsa, D. M.; Baldi, A.; Pasturel, M.; Schreuders, H.; Dam, B.; Griessen, R.; Vermeulen, P.; Notten, P. H. L. Mg−Ti−H Thin Films for Smart Solar Collectors. *Appl. Phys. Lett.* **2006**, *88* (24), 241910.
(16) Bagheri, S.; Strohfeldt, N.; Ubl, M.; Berrier, A.; Merker, M.; Richter, G.; Siegel, M.; Giessen, H. Niobium as Alternative Material for Refractory and Active Plasmonics. *ACS Photonics* **2018**, *5* (8), 3298−3304.
(17) Office of Energy Efficiency and Renewable Energy, U.S. Department of Energy. Section 3.7. Hydrogen Safety, Codes and Standards. *Fuel Cell Technologies Office Multi-Year Research, Development, and Demonstration Plan, 2011−2020*; U.S. Department of Energy, 2015.
(18) Adams, B. D.; Chen, A. The Role of Palladium in a Hydrogen Economy. *Mater. Today* **2011**, *14* (6), 282−289.
(19) Penner, R. M. A Nose for Hydrogen Gas: Fast, Sensitive H2 Sensors Using Electrodeposited Nanomaterials. *Acc. Chem. Res.* **2017**, *50* (8), 1902−1910.
(20) Schwarz, R. B.; Khachaturyan, A. G. Thermodynamics of Open Two-Phase Systems with Coherent Interfaces: Application to Metal−Hydrogen Systems. *Acta Mater.* **2006**, *54* (2), 313−323.
(21) Bannenberg, L. J.; Nugroho, F. A. A.; Schreuders, H.; Norder, B.; Trinh, T. T.; Steinke, N.-J.; van Well, A. A.; Langhammer, C.; Dam, B. Direct Comparison of PdAu Alloy Thin Films and Nanoparticles upon Hydrogen Exposure. *ACS Appl. Mater. Interfaces* **2019**, *11* (17), 15489−15497.
(22) Nugroho, F. A. A.; Darmadi, I.; Zhdanov, V. P.; Langhammer, C. Universal Scaling and Design Rules of Hydrogen-Induced Optical Properties in Pd and Pd-Alloy Nanoparticles. *ACS Nano* **2018**, *12* (10), 9903−9912.
(23) Westerwaal, R. J.; Rooijmans, J. S. A.; Leclercq, L.; Gheorghe, D. G.; Radeva, T.; Mooij, L.; Mak, T.; Polak, L.; Slaman, M.; Dam, B.; Rasing, T. Nanostructured Pd−Au Based Fiber Optic Sensors for Probing Hydrogen Concentrations in Gas Mixtures. *Int. J. Hydrogen Energy* **2013**, *38* (10), 4201−4212.
(24) Zhao, Z.; Carpenter, M. A.; Xia, H.; Welch, D. All-Optical Hydrogen Sensor Based on a High Alloy Content Palladium Thin Film. *Sens. Actuators, B* **2006**, *113* (1), 532−538.
(25) Nishijima, Y.; Shimizu, S.; Kurihara, K.; Hashimoto, Y.; Takahashi, H.; Balčytis, A.; Seniutinas, G.; Okazaki, S.; Juodkazyte, J.; Iwasa, T.; Taketsugu, T.; Tominaga, Y.; Juodkazis, S. Optical Readout of Hydrogen Storage in Films of Au and Pd. *Opt. Express* **2017**, *25* (20), 24081−24092.
(26) Zhang, L.; Chang, Q.; Chen, H.; Shao, M. Recent Advances in Palladium-Based Electrocatalysts for Fuel Cell Reactions and Hydrogen Evolution Reaction. *Nano Energy* **2016**, *29*, 198−219.
(27) Coq, B.; Figueras, F. Bimetallic Palladium Catalysts: Influence of the Co-Metal on the Catalyst Performance. *J. Mol. Catal. A: Chem.* **2001**, *173* (1), 117−134.
(28) Sarina, S.; Zhu, H.; Jaatinen, E.; Xiao, Q.; Liu, H.; Jia, J.; Chen, C.; Zhao, J. Enhancing Catalytic Performance of Palladium in Gold and Palladium Alloy Nanoparticles for Organic Synthesis Reactions through Visible Light Irradiation at Ambient Temperatures. *J. Am. Chem. Soc.* **2013**, *135* (15), 5793−5801.
(29) Coulter, K. E.; Way, J. D.; Gade, S. K.; Chaudhari, S.; Alptekin, G. O.; DeVoss, S. J.; Paglieri, S. N.; Pledger, B. Sulfur Tolerant PdAu and PdAuPt Alloy Hydrogen Separation Membranes. *J. Membr. Sci.* **2012**, *405−406*, 11−19.
(30) Knapton, A. Palladium Alloys for Hydrogen Diffusion Membranes: A Review of High Permeability Materials. *Platinum Metals Rev.* **1977**, *21*, 44−50.
(31) Palm, K. J.; Murray, J. B.; Narayan, T. C.; Munday, J. N. Dynamic Optical Properties of Metal Hydrides. *ACS Photonics* **2018**, *5* (11), 4677−4686.
(32) Murray, J. B.; Palm, K. J.; Narayan, T. C.; Fork, D. K.; Sadat, S.; Munday, J. N. Apparatus for Combined Nanoscale Gravimetric, Stress, and Thermal Measurements. *Rev. Sci. Instrum.* **2018**, *89* (8), No. 085106.
(33) Stoney, G. G. The Tension of Metallic Films Deposited by Electrolysis. *Proc. R. Soc. London, Ser. A* **1909**, *82* (553), 172−175.
(34) EerNisse, E. P. Simultaneous Thin-Film Stress and Mass-Change Measurements Using Quartz Resonators. *J. Appl. Phys.* **1972**, *43* (4), 1330−1337.
(35) Johnson, P. B.; Christy, R. W. Optical Constants of Transition Metals: Ti, V, Cr, Mn, Fe, Co, Ni, and Pd. *Phys. Rev. B* **1974**, *9* (12), 5056−5070.
(36) Johnson, P. B.; Christy, R. W. Optical Constants of the Noble Metals. *Phys. Rev. B* **1972**, *6* (12), 4370−4379.
(37) Kadkhodazadeh, S.; Nugroho, F. A. A.; Langhammer, C.; Beleggia, M.; Wagner, J. B. Optical Property−Composition Correlation in Noble Metal Alloy Nanoparticles Studied with EELS. *ACS Photonics* **2019**, *6* (3), 779−786.
(38) Nishijima, Y.; Hashimoto, Y.; Seniutinas, G.; Rosa, L.; Juodkazis, S. Engineering Gold Alloys for Plasmonics. *Appl. Phys. A: Mater. Sci. Process.* **2014**, *117* (2), 641−645.
(39) Yamada, Y.; Tajima, K.; Bao, S.; Okada, M.; Yoshimura, K. Hydrogenation and Dehydrogenation Processes of Palladium Thin Films Measured in Situ by Spectroscopic Ellipsometry. *Sol. Energy Mater. Sol. Cells* **2009**, *93* (12), 2143−2147.
(40) Maeland, A.; Flanagan, T. B. X-Ray and Thermodynamic Studies of the Absorption of Hydrogen by Gold-Palladium Alloys. *J. Phys. Chem.* **1965**, *69* (10), 3575−3581.
(41) Hydrogen in Metals I: Basic Properties. In *Topics in Applied Physics*; Alefeld, G., Völkl, J., Eds.; Springer-Verlag: Berlin, Heidelberg, 1978.
(42) Hydrogen in Metals II: Application-Oriented Properties. In *Topics in Applied Physics*; Alefeld, G., Völkl, J., Eds.;Springer-Verlag: Berlin, Heidelberg, 1978.
(43) Bucur, R. V.; Mecea, V.; Flanagan, T. B. The Kinetics of Hydrogen (Deuterium) Sorption by Thin Palladium Layers Studied with a Piezoelectric Quartz Crystal Microbalance. *Surf. Sci.* **1976**, *54* (2), 477−488.
(44) Feenstra, R.; de Groot, D. G.; Rector, J. H.; Salomons, E.; Griessen, R. Gravimetrical Determination of Pressure-Composition Isotherms of Thin PdH c Films. *J. Phys. F: Met. Phys.* **1986**, *16* (12), 1953.
(45) Łukaszewski, M.; Kuśmierczyk, K.; Kotowski, J.; Siwek, H.; Czerwiński, A. Electrosorption of Hydrogen into Palladium-Gold Alloys. *J. Solid State Electrochem.* **2003**, *7* (2), 69−76.
(46) Hubkowska, K.; Łukaszewski, M.; Czerwiński, A. Influence of Temperature on Hydrogen Electrosorption into Palladium−Noble Metal Alloys. Part 1: Palladium−Gold Alloys. *Electrochim. Acta* **2010**, *56* (1), 235−242.
(47) Pivak, Y.; Schreuders, H.; Slaman, M.; Griessen, R.; Dam, B. Thermodynamics, Stress Release and Hysteresis Behavior in Highly Adhesive Pd−H Films. *Int. J. Hydrogen Energy* **2011**, *36* (6), 4056−4067.
(48) Wagner, S.; Pundt, A. Quasi-Thermodynamic Model on Hydride Formation in Palladium−Hydrogen Thin Films: Impact of Elastic and Microstructural Constraints. *Int. J. Hydrogen Energy* **2016**, *41* (4), 2727−2738.
(49) Gremaud, R.; Gonzalez-Silveira, M.; Pivak, Y.; de Man, S.; Slaman, M.; Schreuders, H.; Dam, B.; Griessen, R. Hydrogenography of PdHx Thin Films: Influence of H-Induced Stress Relaxation Processes. *Acta Mater.* **2009**, *57* (4), 1209−1219.
(50) Baldi, A.; Mooij, L.; Palmisano, V.; Schreuders, H.; Krishnan, G.; Kooi, B. J.; Dam, B.; Griessen, R. Elastic versus Alloying Effects in Mg-Based Hydride Films. *Phys. Rev. Lett.* **2018**, *121* (25), 255503.
(51) Ham, B.; Junkaew, A.; Arróyave, R.; Park, J.; Zhou, H.-C.; Foley, D.; Rios, S.; Wang, H.; Zhang, X. Size and Stress Dependent Hydrogen Desorption in Metastable Mg Hydride Films. *Int. J. Hydrogen Energy* **2014**, *39* (6), 2597−2607.

DOI: 10.1021/acsami.9b14244
ACS Appl. Mater. Interfaces 2019, 11, 45057−45067

(52) Chung, C.-J.; Lee, S.-C.; Groves, J. R.; Brower, E. N.; Sinclair, R.; Clemens, B. M. Interfacial Alloy Hydride Destabilization in Mg/Pd Thin Films. *Phys. Rev. Lett.* **2012**, *108* (10), 106102.
(53) Dornheim, M.; Pundt, A.; Kirchheim, R.; Molen, S. J. v. d.; Kooij, E. S.; Kerssemakers, J.; Griessen, R.; Harms, H.; Geyer, U. Stress Development in Thin Yttrium Films on Hard Substrates during Hydrogen Loading. *J. Appl. Phys.* **2003**, *93* (11), 8958−8965.
(54) Wagner, S.; Klose, P.; Burlaka, V.; Nörthemann, K.; Hamm, M.; Pundt, A. Structural Phase Transitions in Niobium Hydrogen Thin Films: Mechanical Stress, Phase Equilibria and Critical Temperatures. *ChemPhysChem* **2019**, *20*, 1890−1904.
(55) Li, J.; Kamin, S.; Zheng, G.; Neubrech, F.; Zhang, S.; Liu, N. Addressable Metasurfaces for Dynamic Holography and Optical Information Encryption. *Sci. Adv.* **2018**, *4* (6), eaar6768.
(56) Farinha, T. G.; Gong, C.; Benson, Z. A.; Leite, M. S. Magnesium for Transient Photonics. *ACS Photonics* **2019**, *6* (2), 272−278.

DOI: 10.1021/acsami.9b14244
ACS Appl. Mater. Interfaces 2019, 11, 45057−45067